

Electrical characterization of fully encapsulated ultra thin black phosphorus-based heterostructures with graphene contacts

Ahmet Avsar¹, Ivan J. Vera-Marun^{1,2}, Tan Jun You¹, Kenji Watanabe³, Takashi Taniguchi³ Antonio H. Castro Neto¹ and Barbaros Özyilmaz^{1,4,†}

¹Graphene Research Center & Department of Physics, 2 Science Drive 3, National University of Singapore, Singapore 17542, Singapore

²Physics of Nanodevices, Zernike Institute for Advanced Materials, University of Groningen, Nijenborgh 4, 9747 AG, Groningen, The Netherlands

³National Institute for Materials Science, 1-1 Namiki, Tsukuba 305-0044, Japan

⁴Nanocore, 4 Engineering Drive 3, National University of Singapore, Singapore 117576, Singapore

[†]Corresponding author: barbaros@nus.edu.sg,

The presence of finite bandgap and high mobility in semiconductor few-layer black phosphorus offers an attractive prospect for using this material in future two-dimensional electronic devices. Here we demonstrate for the first time fully encapsulated ultrathin (down to bilayer) black phosphorus field effect transistors in Van der Waals heterostructures to preclude their stability and degradation problems which have limited their potential for applications. Introducing monolayer graphene in our device architecture for one-atom-thick conformal source-drain electrodes enables a chemically inert boron nitride dielectric to tightly seal the black phosphorus surface. This architecture, generally applicable for other sensitive two-dimensional crystals, results in stable transport characteristics which are hysteresis free and identical both under high vacuum and ambient conditions. Remarkably, our graphene electrodes lead to contacts not dominated by thermionic emission, solving the issue of Schottky barrier limited transport in the technologically relevant two-terminal field effect transistor geometry.

KEYWORDS Black phosphorus, graphene, work-function, Schottky barrier, encapsulation, hysteresis

Monolayer black phosphorus (BP) or phosphorene, a one atom thick sheet of phosphorus atoms arranged in a puckered structure, has recently emerged as a potential candidate to address the shortcomings of previously studied 2D materials¹⁻⁴. Few-layer BP can be easily cleaved from bulk crystals due to weak interlayer van der Waals interaction. Its transport properties depend strongly on the thickness of the obtained crystals and it has a direct band gap, increasing monotonically from ~ 0.3 eV in bulk to ~ 1.7 eV in phosphorene⁵. These properties, together with recent observations of high mobilities up to $1,000 \text{ cm}^2/\text{V}\cdot\text{s}$ ^{1,3,4} at room temperature (one order of magnitude higher than previous semiconducting 2Ds⁶) make BP suitable for applications such as fast and broadband photodetectors⁷, solar cells⁸ and digital electronics¹.

The cornerstone of digital electronics is the field effect transistor (FET), which consists of an active semiconductor where charge carriers flow between source and drain electrodes and an electrostatic gate modulating the carrier density in the channel. For practical applications, the source and drain electrodes are expected to exhibit low contact resistances and linear responses, while the

semiconducting channel should be stable over time. FETs using BP channel exhibited high on/off ratios^{1,2,4,9}, low subthreshold swings^{1,10} and excellent current saturations^{1,4} making BP attractive for the device applications. However the preparation of BP-based devices for such FET applications still poses challenges. The BP channel tends to degrade after a short exposure to air due to a photo-activated charge transfer process¹¹. This degradation causes an increase in surface roughness and presence of chemisorbed species leading to gap states in BP¹². The resulting non-ideal interfaces, together with the presence of large Schottky barriers common in the physics of metal/semiconductor contacts set limitations for the performance of BP FETs. When transport across the contacts is dominated by the thermionic emission due to large Schottky barrier height, rather than tunneling, the charge injection efficiency is severely limited due to large contact resistances and a highly non-linear response.

We offer a complete solution to the challenges mentioned above by creating a 2D heterostructure where all interfaces are based on van der Waals bonding¹³. Towards this, we have contacted atomically thin layers of BP with monolayer graphene and fully encapsulated the device with hexagonal boron nitride (h-BN) in a layer-by-layer fashion, all under an inert argon environment with negligible water and oxygen contents. Introducing graphene as a conformal, one-atom-thick crystal, allows the ultrathin h-BN crystal to fully conform to the underlying structure without leaving any space for air or other species to diffuse. It is worth noting that utilizing regularly used metal contacts rather than monolayer graphene does not allow a full sealing even they are encapsulated with h-BN layer (See Supplementary Information). Such a perfect encapsulation leads to the observation of equally good performances under both ambient and vacuum conditions with hysteresis free characteristics in our pristine heterostructures. Integration of graphene electrodes with tunable work-function¹⁴ enables enhanced charge injection efficiency into BP through low contact resistance interfaces with negligible Schottky barriers not dominated by thermionic emission but by tunneling essential for practical FET applications. Our results are important milestone towards fabrication of high quality BP devices relevant for operation under ambient conditions and room temperature.

The device fabrication starts with etching of mechanically exfoliated monolayer graphene flakes into isolated contact stripes by using standard electron beam lithography and oxygen plasma techniques. Few layers of h-BN crystal are partially deposited onto these monolayer graphene stripes with a dry transfer method^{15,16}. The graphene/h-BN stack is isolated from the wafer with a KOH etching process. Meanwhile, a thin BP crystal is exfoliated onto SiO₂ (300nm)/Si wafer in an argon environment, followed by the transfer of the graphene/h-BN stack onto this freshly exfoliated BP crystal. We take care that h-BN fully encapsulates the BP crystal. During the device fabrication process, the surface of BP has never been exposed to air. Fabrication is completed with forming Cr/Au (2nm/80nm) electrodes on non-encapsulated regions of the graphene stripes and on top of the h-BN crystal, for serving as source-drain and top gate electrodes, respectively. A more detailed description of the device fabrication is discussed in the supplementary information.

Optical images of the device before and after the metallization process are shown in Figure 1-a and Figure 1-b, respectively. The final device is annealed at 340 C under high vacuum conditions. This annealing step is crucial to obtain high quality contacts. Firstly, the annealing treatment improves the bonding of graphene and h-BN layers to the BP crystal by removing the small bubbles that might be formed during the transfer process¹⁵. Secondly, it removes the possible adsorbants present at the interface of BP and SiO₂ that can cause significant hysteresis in transport measurements¹⁷. AFM images confirm that the device is clean and free of wrinkles (See Supplementary Information). The resulting heterostructure is illustrated schematically in Figure 1-c. Raman spectrum for the encapsulated BP device is shown in Figure 1-d where the characteristic¹⁸ A_g¹, B_{2g} and A_g² peaks of BP are clearly visible at the wave numbers of 362.6, 439.8 and 467.4, respectively. We do not observe any obvious change in Raman spectrum before and after annealing at 340 C, implying that the encapsulating h-BN crystal effectively protects BP. It is worth noting that non-encapsulated BP crystals are observed to degrade during the annealing process (See supplementary Information). Electronic transport measurements are carried out in two-terminal configuration under ambient and vacuum conditions ($\sim 1 \times 10^{-7}$ Torr). In this

work, we studied a total of three samples and present representative data on two encapsulated BP devices with the thickness of ~ 4.5 nm (6 layer, sample S1) and ~ 1.6 nm (2 layer, sample S2) respectively. Unless otherwise stated, the results obtained in the relatively thicker sample are discussed in the manuscript. SiO₂ (~ 300 nm) and h-BN (~ 16 nm) dielectrics are utilized to apply back and top gate biases (V_{BG} and V_{TG}) respectively (See Figure 2-a). The bias current (I_{SD}) of BP-based devices is characterized as a function of source-drain voltage (V_{SD}), temperature (T), V_{BG} and V_{TG} .

Now we discuss the transport characteristics of our encapsulated device measured under both vacuum and ambient conditions. For comparison, we also fabricated a non-encapsulated device with similar thickness of BP crystal (Insets of Figure 2-b and 2-c). Figure 2-b shows the V_{TG} dependence of I_{SD} at fixed V_{BG} (-40 V) and V_{SD} (100 meV) under vacuum conditions. While the non-encapsulated device shows a significant hysteresis (~ 30 V) even under vacuum conditions, the encapsulated device has nearly hysteresis free transport characteristics. In general, such positive hysteresis is caused by the sensitivity of 2D crystals to the external chemical environments at the top surface and with the hosting substrate (See supplementary information)^{17,19}. In our device, the first is excluded as the device is fully encapsulated. The second potential source is also eliminated due to the high temperature annealing treatment during device fabrication. The stability of our device architecture is evidenced by noting that the device shows this hysteresis free transport behavior even two months after the device is fabricated (See supplementary information). Next, we discuss the transport performance under ambient conditions. As can be seen in Figure 2-c, the encapsulated device has nearly identical output characteristics under both ambient and vacuum conditions. On the other hand, for the non-encapsulated device we observe a significant drop in the conductivity (up to 80%) at ambient conditions (Inset Figure 2-c), resulting in lower field effect mobility and current modulation (See supplementary Information). These observations clearly indicate that the high quality h-BN encapsulating layer together with monolayer graphene electrodes protect the BP surface from interaction with air. Compared to other passivation schemes such as SiO₂, PMMA and ALD grown dielectrics of Al₂O₃ and HfO₂; h-BN is intrinsically inert and pinhole

free^{20,21}. This minimizes the possible oxidation of BP through pinholes in the dielectric and also any chemical reaction. It was recently shown that the water precursor in ALD grown Al₂O₃ causes hysteresis in MoS₂-based FETs^{19,22}. Such effect will be more dramatic in BP based devices as the crystal is very sensitive to the adsorbed oxygen in water.²³ On the contrary, the interface in our heterostructure device is pristine as demonstrated by the lack of hysteresis and the stability discussed above.

Now we turn our attention to the equally important contact resistance aspect of our device. Figure 3-a-c show the 2D color plots of I_{SD} as a function of V_{SD} and V_{BG} at V_{TG} = -4V, 0V, 4V respectively. The device shows p-type behavior even at V_{TG}= 4V. However, the application of V_{TG} causes a clear shift in the threshold region which starts to be observed at more positive V_{BG} values as V_{TG} is changed from positive to negative values. Also note that I_{SD} shows a tendency of saturation at high negative V_{BG} values. To elucidate this behavior, we plotted the V_{BG} dependence of I_{SD} at V_{SD} = 0.1V for V_{TG} = -4V, 0V, 4V (Figure 3-d). While we see similar saturation behavior for each values of V_{TG}, the magnitude of the saturation current increases as the V_{TG} is tuned from positive to negative values. It has been extensively discussed that the saturation current in 2D semiconductors-based FETs is dominated by the contact resistance in a two-terminal FET structure with only a minor contribution in our case of graphene and BP channels⁴. Therefore the observation of the increase in the saturation current as the V_{TG} is changed from 4V to -4V clearly indicates that contact quality is improved. To quantify this, the total resistance vs V_{BG} curve is extrapolated as suggested by R. Toy et al. by using the polynomial $A+B/x+C/x^2$ where the fitting parameter A refers to the contribution of the contact resistance to the total device resistance at high gate biases where the channel resistance is substantially small²⁴. We observe a sharp decrease in the magnitude of the contact resistance from ~46 kΩ to ~ 15.8 kΩ by only changing the V_{TG} from 4V to -4V. This is the same magnitude with the one obtained from the stable MoS₂-based heterostructure device which is similarly contacted and encapsulated with graphene and h-BN, respectively²⁴. Such improvement is because of the unique work-function tunability of graphene electrodes which allows for a higher efficiency of hole injection to the valance band of BP

at high electric fields.¹⁴ Here, having V_{TG} together with V_{BG} in our device allows us to modulate the graphene work function more effectively compared to the one that can be achieved only with V_{BG} . As schematically shown in Figure 3-f, the application of large negative displacement fields (both V_{TG} and V_{BG} are negative) shifts the Fermi level of graphene towards the valence band of BP. The conduction and valence bands are bent upwards, making it easier to inject holes from graphene source-drain electrodes to BP. The relation between I_{SD} and V_{SD} gives additional information about the Schottky barrier heights. As shown in Figure 3-e, I_{SD} - V_{SD} is slightly non-linear at small displacement fields ($V_{TG} = 4V$, $V_{BG} = -30V$). However, it becomes more linear as V_{TG} is swept to 0V and eventually we observe a perfectly linear relation upon the application of large displacement fields ($V_{TG} = 4V$, $V_{BG} = -30V$). This observation gives independent proof for the reduced Schottky barrier at the source-drain interfaces. It is also worth noting that both encapsulated and non-encapsulated BP devices with Ti/Au contacts have non-linear I_{SD} - V_{SD} behavior even at low V_{SD} values in sharp contrast to this graphene contacted device (See supplementary information).

In order to determine the nature of the graphene/BP interfaces, we carried out a detailed study of I_{SD} as a function of temperature. Figure 4-a shows the V_{SD} and T dependence of I_{SD} at large displacement fields ($V_{BG} = -70$ V and $V_{TG} = -4$ V). We observe the linear relation between I_{SD} and V_{SD} at both current polarities for all temperature. Remarkably, the change in I_{SD} is less than 10% within the temperature range of 300 K to 10 K at high bias regime. This shows that thermionic emission is not the dominant transport mechanism in these graphene contacted BP devices. To confirm this, we analyze the data using the thermionic emission model describing the charge transport through a schottky barrier into the BP channel

$$I_{SD} = AA^*T^{1.5} \exp \left[-\frac{e}{k_B T} \left(\Phi_B - \frac{V_{SD}}{n} \right) \right]$$

where A is the contact area, A^* is the 2D Richardson constant, e is the electron charge, k_B is the Boltzmann constant and Φ_B is the Schottky barrier height and n is the ideality factor²⁵. Figure 4-b shows the Arrhenius plot ($\ln(I_{SD}/T^{1.5})$ vs $1000/T$) for source-drain bias voltages varying from 1 V to 0.1 V at fixed $V_{BG}=-70$ V and $V_{TG}=-4$ V. The Arrhenius plot has two distinct linear temperature regimes of high (60K-300K) and low (10K-60K) temperature. The intercepts (S_0) of slope vs V_{SD} plot allow extracting the Schottky barrier height (Φ_B) by using $\Phi_B = -10^3 S_0 k_B / q$ (See supplementary information).²⁵ All the extracted Schottky barrier height values are found to be small and negative, ranging from -17 meV to -2.5 meV. This indicates that thermionic emission does not dominate the transport in our devices. It is worth noting that these observations persist for each V_{BG} values (See supplementary Information). As schematically illustrated in Figure 4-c, charge injection into semiconductors is dominated by tunneling (direct or thermally assisted) or thermionic emission. In contrast to a recent report on TiO_2/Co contacted BP device¹⁰ which has charge injection dominated by thermionic emission, the nearly temperature insensitivity of I_{SD} in our device suggests that charge injection is rather dominated by tunneling. Therefore our improved contacts should have significant impact on the transport in two terminal BP-based FETs. To demonstrate the latter, we show in Figure 4-d the temperature dependence of the mobility. The device demonstrates remarkable temperature stability. While a previous report on Ti/Au contacted BP device⁴ has shown a decrease in mobility of more than 80% in a two-terminal measurement configuration as the temperature is reduced from RT to 20 K, our device shows a negligible decrease of mobility from RT down to 100 K (~10%) and only a moderate decrease down to 10 K (~30%). We note that temperature dependence of the mobility is even weaker at higher V_{SD} values as discussed before and shown in inset of Figure 4-a. Observation of such a weak temperature dependence of the mobility is further demonstration of the negligible Schottky barrier height, and is potentially useful for achieving subthreshold swing below the kT/q thermal limit of 60 mV/decade at room temperature²⁶ in BP-based FETs if the dielectric is engineered (See supplementary information).

Finally we remark that our device architecture allows us to study very thin layers of BP, otherwise very challenging due to the issue of its rapid degradation. The recent prediction of band gap modulation in dual gated bilayer BP device⁸ make our approach attractive for the perspective of fundamental science as well. Towards this, we utilized our encapsulated device architecture to study the transport properties of a bilayer BP-FET device. Figure 5 shows the V_{BG} dependence of I_{SD} at fixed $V_{SD} = 0.1$ V. Similar to the previously shown device, bilayer BP-based FET also shows a dominant p-type behavior. However, we achieve a clear bipolar behavior where both electron and hole conduction are observed. This result is consistent with a strongly reduced electric field screening in such ultra thin samples²⁷. In this device, we observe an on/off ratio of ~ 100 and a sub-threshold swing of ~ 30 V and ~ 17 V per decade at hole and electron conduction side respectively at room temperature. While this sub-threshold swing value is comparable to the previous results obtained with similar SiO_2 dielectric thicknesses^{1,10}, we note that improved sub-threshold swing values are obtained in thicker BP samples (See supplementary information). Field effect mobilities of ~ 120 $\text{cm}^2/\text{V.s}$ at hole side and ~ 40 $\text{cm}^2/\text{V.s}$ at electron side are extracted in this encapsulated bilayer BP device by using^{1,2,4}

$$\mu = \frac{L}{W} \frac{1}{C_{OX}} \frac{1}{V_{SD}} \frac{\partial I_{SD}}{\partial V_{SD}}$$

where μ is the field effect mobility, L and W are the length and width of measured junction respectively, $C_{OX} = \frac{\epsilon\epsilon_{OX}}{d}$ is the capacitance of SiO_2 substrate. The enhanced gate tunability now allows us to tune the graphene work-function more effectively even with V_{BG} alone and as a result, a linear I_{DS} - V_{DS} relation is achieved even at high V_{SD} values (Inset Figure 5). We note that unlike previously studied semiconducting 2D crystals^{28,29}, the encapsulation and enhanced graphene contacts do not improve the mobility of the encapsulated devices compared to non-encapsulated devices significantly. This suggests that the mobility is limited by the SiO_2 substrate rather than either the adsorbants present in air nor high Schottky barrier heights as previously suggested^{1,4}.

In conclusion, we report the fabrication of a new device architecture that allows charge transport studies in ultra thin BP crystals reliably by utilizing monolayer graphene and ultra thin h-BN as source-drain contacts and encapsulating layer. We demonstrate that these devices are extremely robust to the environment and hysteresis is nearly eliminated. Utilizing work-function tunable graphene electrodes into our heterostructure reduces the Schottky barrier height significantly, with current injection dominated by tunneling rather than thermionic emission. Our findings provide an important step toward fundamental and applied studies in few layers of BP-based FET as well as give access to study the transport properties of other sensitive crystals such as silicene³⁰ and GaSe³¹.

ACKNOWLEDGEMENTS

We thank J. Balakrishnan, E. C. T. O'Farrell, T. Taychatanapat and S. Natarajan for their help and useful discussions. B. Ö. would like to acknowledge support by the National Research Foundation, Prime Minister's Office, the Singapore under its Competitive Research Programme (CRP Award No. NRF-CRP9-2011-3), the Singapore National Research Foundation Fellowship award (RF2008-07), and the SMF-NUS Research Horizons Award 2009-Phase II. A.H.C.N. would like to acknowledge support by the National Research Foundation, Prime Minister's Office, Singapore under its Competitive Research Programme (CRP Award No. NRF-CRP6-2010-5). I. J. V. M. would like to acknowledge support by the Netherlands Organisation for Scientific Research (NWO).

REFERENCES

- (1) Li, L.; Yu, Y.; Ye, G. J.; Ge, Q.; Ou, X.; Wu, H.; Feng, D.; Chen, X. H.; Zhang, Y. *Nat. Nanotechnol.* **2014**, *9*, 372–377.
- (2) Koenig, S. P.; Doganov, R. A.; Schmidt, H.; Castro Neto, A. H.; Özyilmaz, B. *Appl. Phys. Lett.* **2014**, *104*, 103106.
- (3) Xia, F.; Wang, H.; Jia, Y. *Nat. Commun.* **2014**, *5*, 4458.
- (4) Liu, H.; Neal, A. T.; Zhu, Z.; Luo, Z.; Xu, X.; Tománek, D.; Ye, P. D. *ACS Nano* **2014**, *8*, 4033–4041.

- (5) Tran, V.; Soklaski, R.; Liang, Y.; Yang, L. *Phys. Rev. B* **2014**, *89*, 235319.
- (6) Wang, Q. H.; Kalantar-Zadeh, K.; Kis, A.; Coleman, J. N.; Strano, M. S. *Nat. Nanotechnol.* **2012**, *7*, 699–712.
- (7) Buscema, M.; Groenendijk, D. J.; Blanter, S. I.; Steele, G. A.; van der Zant, H. S. J.; Castellanos-Gomez, A. *Nano Lett.* **2014**, *14*, 3347–3352.
- (8) Dai, J.; Zeng, X. C. *J. Phys. Chem. Lett.* **2014**, *5*, 1289–1293.
- (9) Qiao, J.; Kong, X.; Hu, Z.-X.; Yang, F.; Ji, W. *Nat. Commun.* **2014**, *5*, 4475.
- (10) Kamalakar, M. V.; Madhushankar, B. N.; Dankert, A.; Dash, S. P. arXiv:1406.4476, **2014**.
- (11) Favron, A.; Gaufres, E.; Fossard, F.; Lévesque, P. L.; Phaneuf-L'Heureux, A.-L.; Tang, N. Y.-W.; Loiseau, A.; Leonelli, R.; Francoeur, S.; Martel, R. arXiv:1408.0345, **2014**.
- (12) Leong, W. S.; Luo, X.; Li, Y.; Khoo, K. H.; Quek, S. Y.; Thong, J. T. L. arXiv:1410.1328, **2014**.
- (13) Geim, A. K.; Grigorieva, I. V. *Nature* **2013**, *499*, 419–425.
- (14) Yu, Y.-J.; Zhao, Y.; Ryu, S.; Brus, L. E.; Kim, K. S.; Kim, P. *Nano Lett.* **2009**, *9*, 3430–3434.
- (15) Avsar, A.; Tan, J. Y.; Taychatanapat, T.; Balakrishnan, J.; Koon, G. K. W.; Yeo, Y.; Lahiri, J.; Carvalho, A.; Rodin, A. S.; O'Farrell, E. C. T.; Eda, G.; Castro Neto, A. H.; Ozyilmaz, B. *Nat. Commun.* **2014**, *5*, 4875.
- (16) Mayorov, A. S.; Gorbachev, R. V.; Morozov, S. V.; Britnell, L.; Jalil, R.; Ponomarenko, L. A.; Blake, P.; Novoselov, K. S.; Watanabe, K.; Taniguchi, T.; Geim, A. K. *Nano Lett.* **2011**, *11*, 2396–2399.
- (17) Wang, H.; Wu, Y.; Cong, C.; Shang, J.; Yu, T. *ACS Nano* **2010**, *4*, 7221–7228.
- (18) Castellanos-Gomez, A.; Vicarelli, L.; Prada, E.; Island, J. O.; Narasimha-Acharya, K. L.; Blanter, S. I.; Groenendijk, D. J.; Buscema, M.; Steele, G. A.; Alvarez, J. V.; Zandbergen, H. W.; Palacios, J. J.; van der Zant, H. S. J. *2D Mater.* **2014**, *1*, 025001.
- (19) Late, D. J.; Liu, B.; Matte, H. S. S. R.; Dravid, V. P.; Rao, C. N. R. *ACS Nano* **2012**, *6*, 5635–5641.
- (20) Dean, C. R.; Young, A. F.; Meric, I.; Lee, C.; Wang, L.; Sorgenfrei, S.; Watanabe, K.; Taniguchi, T.; Kim, P.; Shepard, K. L.; Hone, J. *Nat. Nanotechnol.* **2010**, *5*, 722–726.
- (21) Lee, G.-H.; Yu, Y.-J.; Lee, C.; Dean, C.; Shepard, K. L.; Kim, P.; Hone, J. *Appl. Phys. Lett.* **2011**, *99*, 243114.
- (22) Liu, H.; Ye, P. D. *IEEE Electron Device Lett.* **2012**, *33*, 546–548.
- (23) Liu, H.; Neal, A. T.; Si, M.; Du, Y.; Ye, P. D. *IEEE Electron Device Lett.* **2014**, *35*, 795–797.

- (24) Roy, T.; Tosun, M.; Kang, J. S.; Sachid, A. B.; Desai, S. B.; Hettick, M.; Hu, C. C.; Javey, A. *ACS Nano* **2014**, *8*, 6259–6264.
- (25) Chen, J.-R.; Odenthal, P. M.; Swartz, A. G.; Floyd, G. C.; Wen, H.; Luo, K. Y.; Kawakami, R. K. *Nano Lett.* **2013**, *13*, 3106–3110.
- (26) Appenzeller, J.; Knoch, J.; Bjork, M. T.; Riel, H.; Schmid, H.; Riess, W. *IEEE Trans. Electron Devices* **2008**, *55*, 2827–2845.
- (27) Das, S.; Zhang, W.; Demarteau, M.; Hoffmann, A.; Dubey, M.; Roelofs, A. K. *Nano Lett.* **2014**.
- (28) Chuang, H.-J.; Tan, X.; Ghimire, N. J.; Perera, M. M.; Chamlagain, B.; Cheng, M. M.-C.; Yan, J.; Mandrus, D.; Tománek, D.; Zhou, Z. *Nano Lett.* **2014**, *14*, 3594–3601.
- (29) Radisavljevic, B.; Kis, A. *Nat. Mater.* **2013**, *12*, 815–820.
- (30) Molle, A.; Grazianetti, C.; Chiappe, D.; Cinquanta, E.; Cianci, E.; Tallarida, G.; Fanciulli, M. *Adv. Funct. Mater.* **2013**, *23*, 4340–4344.
- (31) Tan, J. Y.; Avsar, A.; Balakrishnan, J.; Koon, G. K. W.; Taychatanapat, T.; O’Farrell, E. C. T.; Watanabe, K.; Taniguchi, T.; Eda, G.; Castro Neto, A. H.; Özyilmaz, B. *Appl. Phys. Lett.* **2014**, *104*, 183504.

FIGURE CAPTIONS

Figure 1. (a) Optical image of the device after the final transfer process. Red and black dashed areas show the black phosphorus crystal and one of the graphene stripes respectively. (b) Optical picture of the device after the contacts are formed. (c) The schematics of the the atomically sharp interfaces in encapsulated BP device. The black, gray, blue and yellow spheres represent the phosphorus, carbon, boron and nitrogen atoms respectively. (d) Raman spectroscopy of few layers of encapsulated black phosphorus flake before and after annealing process.

Figure 2. (a) The schematics of graphene contacted BP device together with the electrical connections for the device characterization. (b) Top gate voltage dependence of bias current in encapsulated device at fixed back gate (-40V) and source-drain (100 meV) biases. Black and red arrows represent the forward and backward gate sweeps. The inset shows the transport curve of a non-encapsulated device.

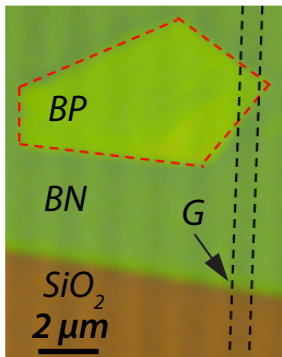
(c) Top gate voltage dependence of bias current under vacuum (black line) and ambient conditions (red line) at fixed back gate (0V) and source-drain (100 meV) biases. The inset shows the gate voltage dependence of a non-encapsulated device. All measurements are performed in ~ 4.5 nm thick sample at room temperature.

Figure 3. (a-c) 2D color fan plot of bias current as a function of back gate and source-drain biases at fixed top gate voltage values of -4V, 0V, 4V respectively. (d) Back gate voltage dependence of bias current at different top gate voltage values. (e) Source-drain voltage dependence of bias current at different displacement fields. Black, red and blue lines represent $V_{TG}=-4V$, 0V and 4V while V_{BG} is fixed to -30V. Inset shows the renormalized values of Figure 3-(e) for more clarity. All measurements are performed in ~ 4.5 nm thick sample at room temperature. (f) Top and bottom schematics illustrate the band alignments at large negative displacement fields and small displacement fields respectively.

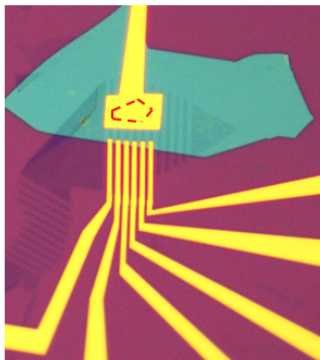
Figure 4. (a) Source-drain bias voltage and temperature dependence of bias current at fixed top gate (-4V) and back gate (-70V) voltage. Inset shows the temperature dependence of bias current at different source-bias voltage values. (b) Arrhenius plot for source-drain voltages from 1V (black sphere) to 0.1V (Dark yellow sphere) at fixed back gate (-70V) and top gate (-4V) voltages. (c) The schematic illustrates current injection from the contact to a p-type semiconductor via tunneling ((1) direct or (2) thermally assisted) and (3) thermionic emission mechanisms. (d) Temperature dependence of two-terminal field effect mobility for the ~ 4.5 nm thick sample.

Figure 5. Back gate voltage dependence of bias current in a bilayer BP-based device at fixed source-drain voltages (0.1V). Inset shows the source-drain voltage dependence of bias current at fixed back gate voltage values. All measurements are performed at room temperature under vacuum conditions.

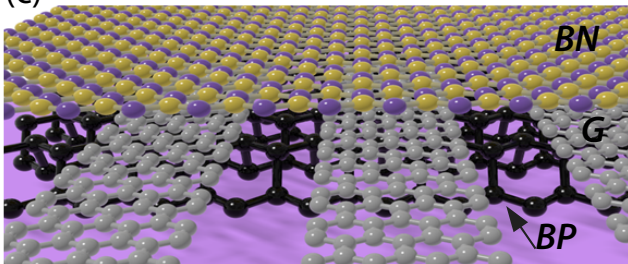
(a)



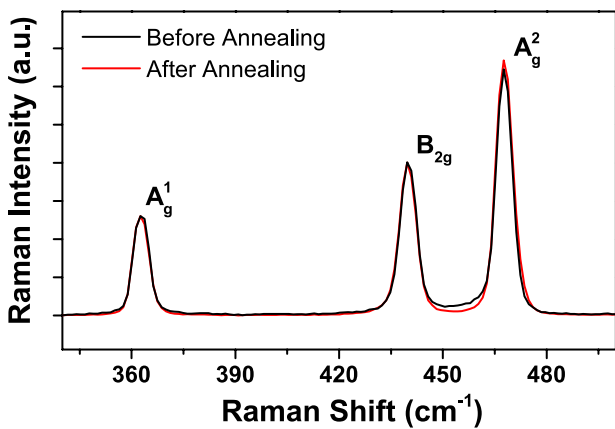
(b)



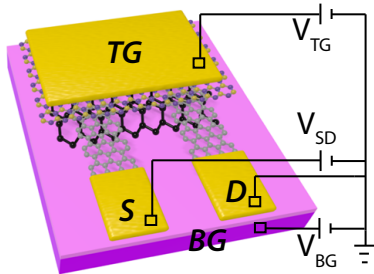
(c)



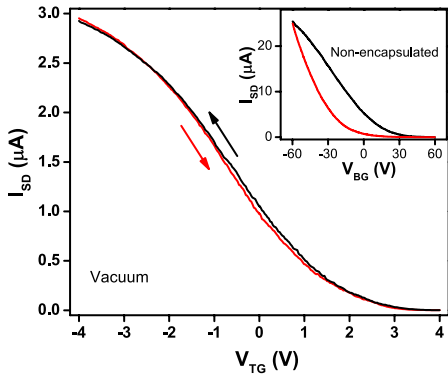
(d)



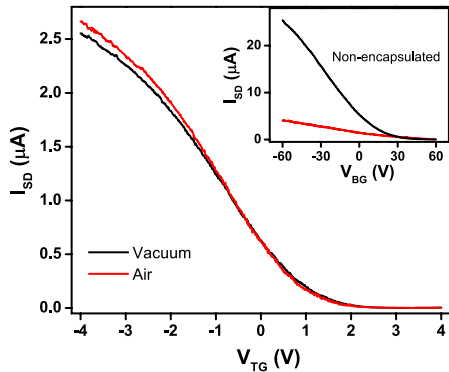
(a)

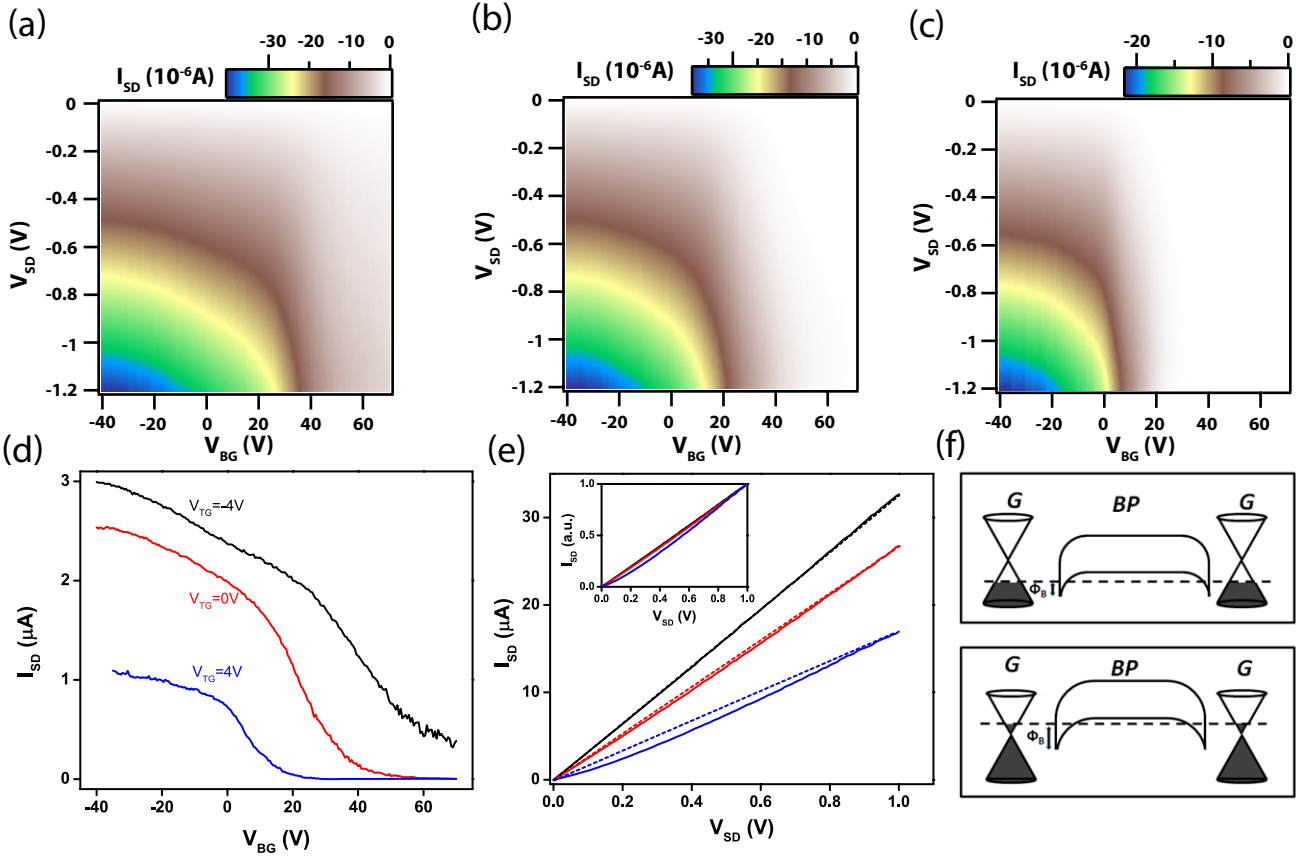


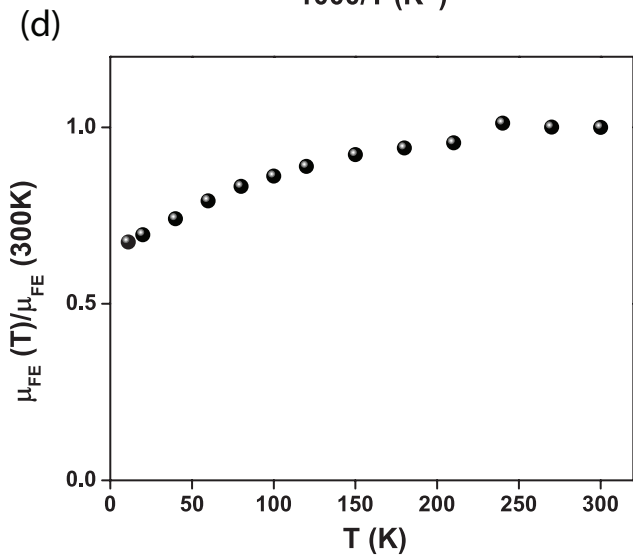
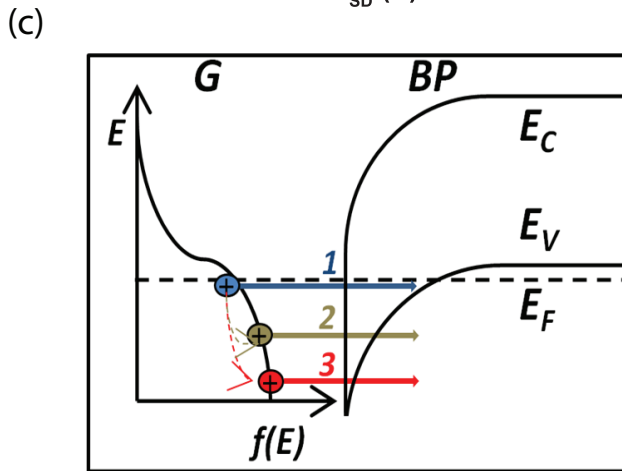
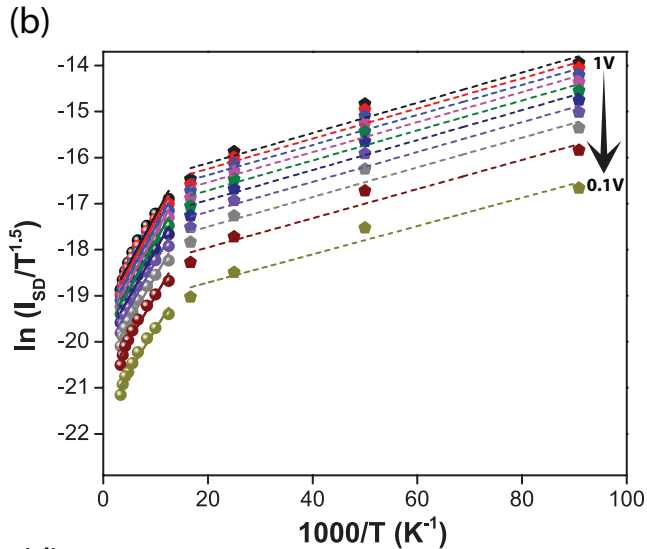
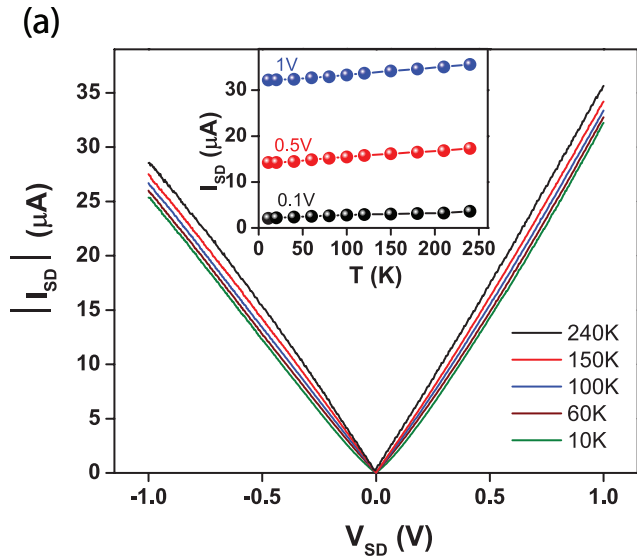
(b)

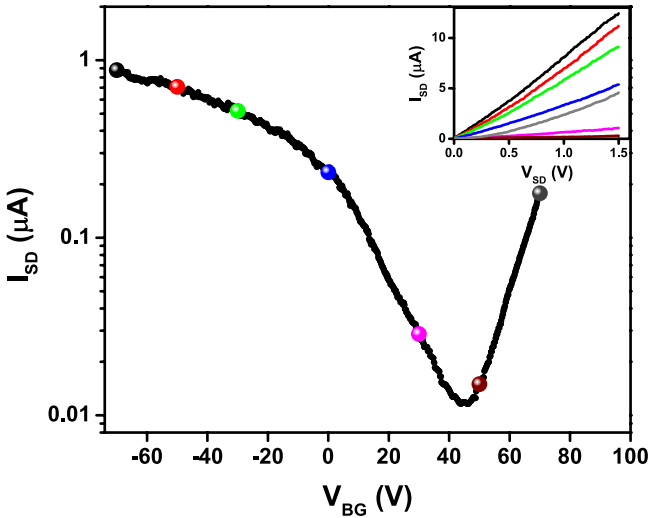


(c)









Supporting Information

Electrical characterization of fully encapsulated ultra thin black phosphorous-based heterostructures with graphene contacts

Ahmet Avsar¹, Ivan J. Vera-Marun^{1, 2}, Tan Jun You¹, Kenji Watanabe³, Takashi Taniguchi³ Antonio H. Castro Neto¹ and Barbaros Özyilmaz^{1,4,†}

¹Graphene Research Center & Department of Physics, 2 Science Drive 3, National University of Singapore, Singapore 17542, Singapore

²Physics of Nanodevices, Zernike Institute for Advanced Materials, University of Groningen, Nijenborgh 4, 9747 AG, Groningen, The Netherlands

³National Institute for Materials Science, 1-1 Namiki, Tsukuba 305-0044, Japan

⁴Nanocore, 4 Engineering Drive 3, National University of Singapore, Singapore 117576, Singapore

†Corresponding author: barbaros@nus.edu.sg,

Section 1: Fabrication process flow

- Graphene is mechanically exfoliated onto Si/SiO₂ (300nm) substrate and etched into stripes to serve as source and drain electrodes.
- Boron Nitride (BN) is exfoliated onto PMMA/PMGI/Si/SiO₂ stack. BN is isolated from the wafer by removing the PMGI resist layer similarly discussed in ref.1.
- BN is transferred partially onto graphene stripes with a dry transfer method by using a home-made transfer stage under ambient conditions (Figure S1-a). The heterostructure is annealed at 340 C under Ar/H₂ gas environment for 6 hours. This process removes the possible polymer residues and small bubbles formed at the graphene/BN interface.
- A thin layer of PMMA is span onto the heterostructure and the resulting G/BN/PMMA stack is isolated from Si/SiO₂ wafer with a KOH etching step (Figure S1-b). The stack is cleaned carefully with DI water.
- BP crystal is exfoliated just before the final transfer process. As shown in Figure S1-c, G/BN/PMMA stack is transferred onto BP crystal in Argon filled glove box (negligible O₂ and H₂O concentration). It is ensured that BN fully encapsulated BP thereby the surface of BP never be exposed to air.
- Cr/Au (2 nm/80 nm) source-drain and top gate contacts are deposited onto non-encapsulated region of graphene and on top of BN crystal, respectively (Figure S1-e).
- The final device is annealed at 340 C under high vacuum conditions to enhance the adhesion between these 2D crystals. The optical and AFM images of final device are shown in Figure S1-f.

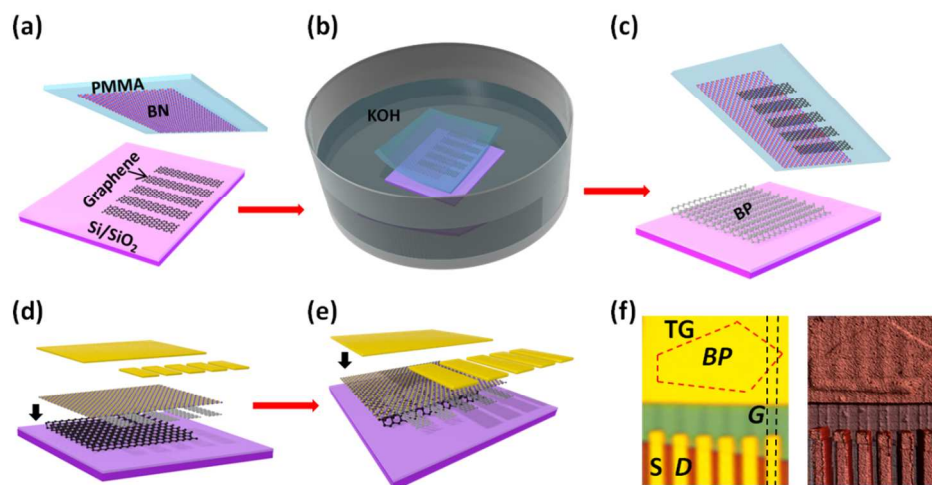


Figure S1: The schematics of device fabrication process for encapsulated black phosphorous device. Process shown at (c) is done under Argon environment. (f) shows the optical and AFM images of the completed device.

Section 2: Effect of annealing on the stability of non-encapsulated black phosphorous crystals

The annealing treatment in our device process is necessary to further improve the performance of the BP-based heterostructures. The annealing treatment is done at 340 C for 3 hours under high vacuum conditions. The encapsulation process with BN crystal physically protects the BP, without showing any signature of the degradation. However, the non-encapsulated BP crystals are very sensitive to the environment. Figure S2-a and S2-b show the optical images of a thin BP crystal before and after annealing process. As clearly can be seen, the non-encapsulated thin flake is fully degraded during the annealing process (Figure S2-c).

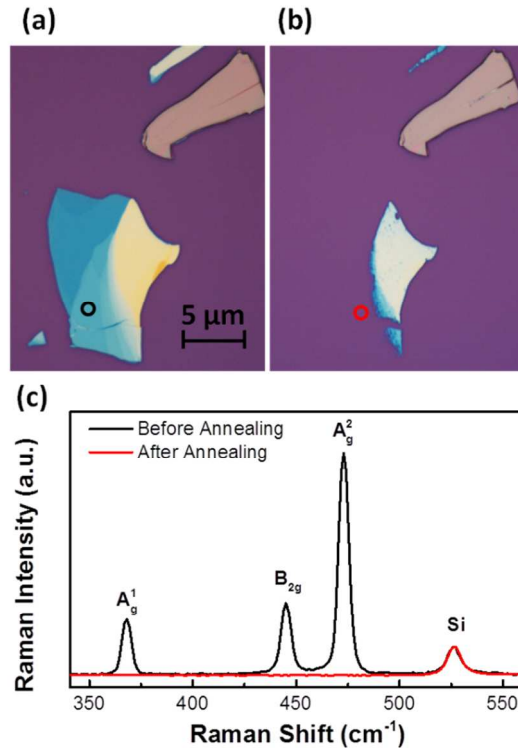


Figure S2: (a-b) Optical images of BP crystal before and after the annealing treatment. Black and red circles represent the Raman spectroscopy locations. (c) Raman spectrum of BP crystal before and after annealing treatment.

Section 3: Hysteresis in non-encapsulated devices

The rapid degradation of non-encapsulated BP crystals at ambient conditions may affect the transport properties of devices substantially. We measured few non-encapsulated devices under both ambient and vacuum conditions at room temperature. Figure S3-a shows the V_{BG} dependence of I_{SD} at fixed V_{SD} (100 meV). The hysteresis increases from $\sim 28V$ to $\sim 60V$ upon exposing the sample to the air. The hysteresis also increases as the V_{BG} range increases. Such trend is caused by a charge trapping mechanism associated with the sensitivity of BP to adsorbents present at air and host substrate¹. Figure S3-c and S3-d show the hysteresis and current modulation ratio in different samples measured under both vacuum and ambient conditions. The thicknesses of flakes in sample 1, 2, 3 and 4 are 5.5 nm, 6 nm, 7 nm and 12 nm, respectively. While we could not make a clear relation between thickness of the crystal and hysteresis, all samples show poorer device performance upon exposing to air. This suggests that passivation of BP devices is critical to obtain reliable and repeatable measurement.

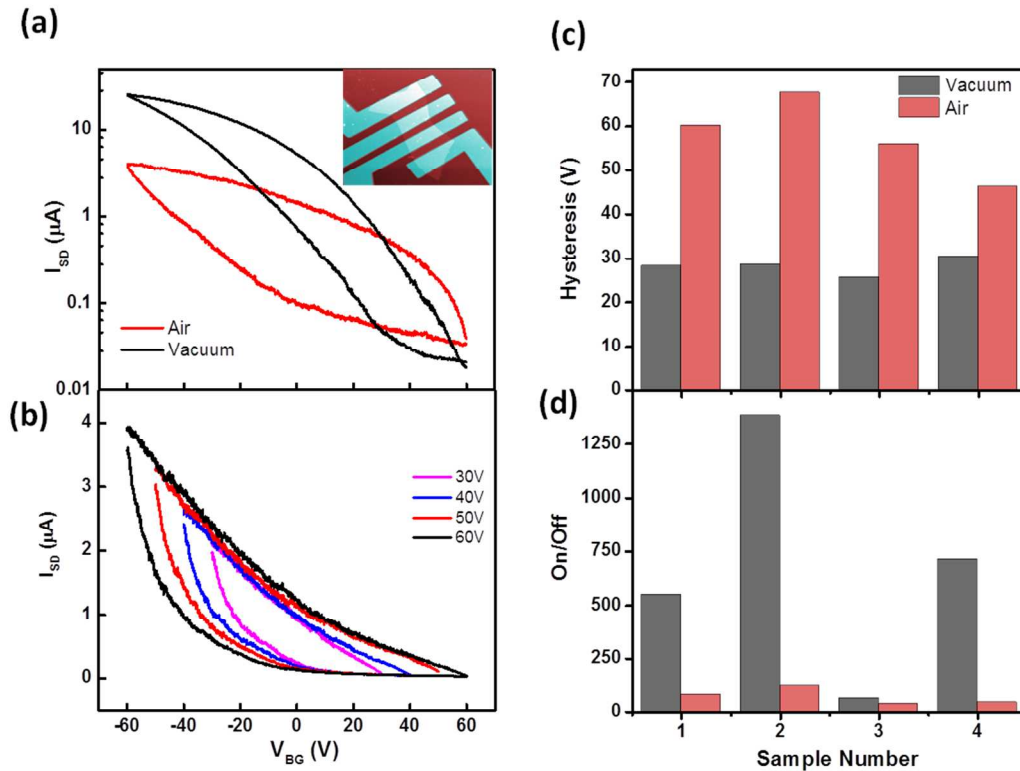


Figure S3: (a) Hysteresis measurement under both vacuum and ambient conditions for a non-encapsulated device (thickness ~ 5.5 nm). Inset is the AFM image of the device. Color height is 0-50 nm. (b) Hysteresis measurement under ambient conditions for different V_{BG} ranges. (c-d) Plots show change in hysteresis and on/off ratios under both ambient and vacuum conditions for different thicknesses samples.

Section 4: Charge transport in a non-encapsulated device at low temperature

The thermal fluctuation at room temperature is in the order of Schottky barrier height for metal contacted devices². This energy allows the charge carriers to overcome the barrier and results in linear I-V relation at room temperature^{3,4}. The linear I-V relation at RT can mislead to believe that an Ohmic contact is achieved. Here we study the transport properties of a metal contacted, non-encapsulated device at 4.2 K. As can be seen in Figure S4-b, the I-V is non-linear at 4.2 K even at low bias voltage. This result is consistent with the work of Kamalakar et al. where they observe a non-linear I-V behavior even at 200 K in metal contacted BP FETs². As discussed earlier, the charge injection in these metal contacted devices is primarily dominated by thermionic emission mechanism. We note that our graphene contacted, encapsulated BP devices have linear I-V even at low temperature and high bias regime.

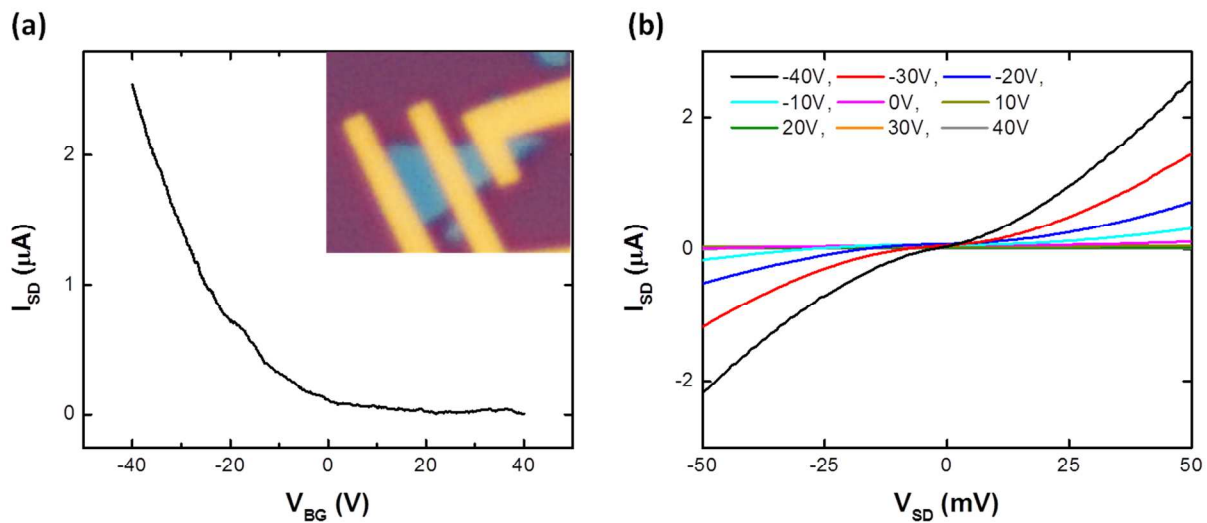


Figure S4: (a) V_{BG} dependence of I_{SD} at fixed V_{SD} (100 meV). The inset shows the optical image of the measured device. (b) V_{SD} dependence of I_{SD} at various V_{BG} values.

Section 5: Robust transport in encapsulated device

Figure S5-a and S5-b show the transport characteristic of an encapsulated device two months after its fabrication was completed. The device shows nearly hysteresis free transport, indicating that BN encapsulation allows reliable operations over time without any signature of the degradation. The I_{SD} is recorded as a function of both V_{BG} and V_{TG} to prove that hysteresis free transport is observed with gating through both the shown hysteresis free transport in main text is not due to thin top gate dielectric.

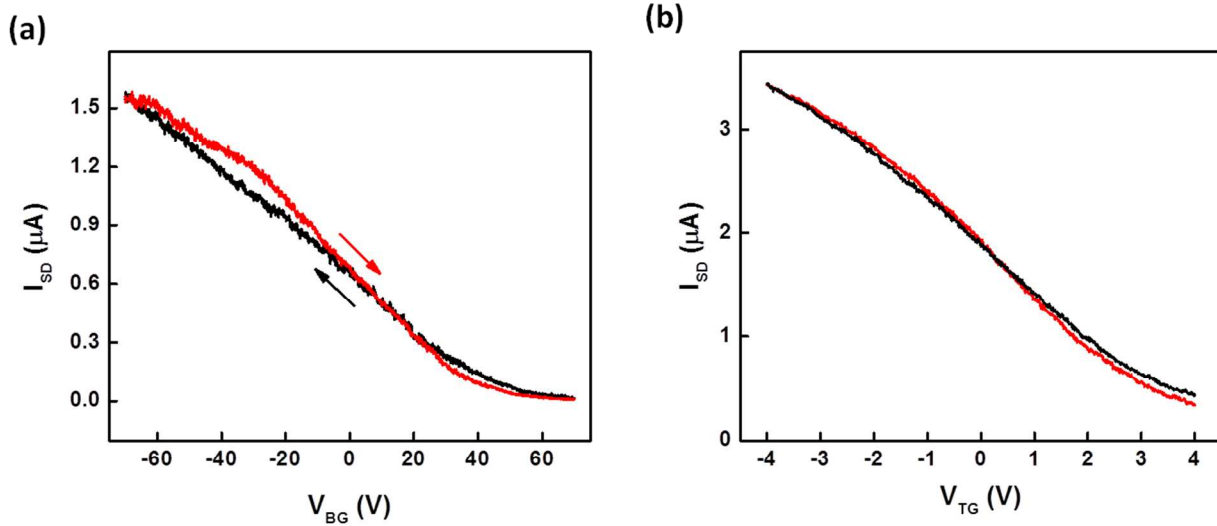


Figure S5: (a) Room temperature V_{BG} dependence of I_{SD} at fixed V_{TG} (0 V) and V_{SD} (100 meV). (b) V_{TG} dependence of I_{SD} at fixed V_{BG} (-70 V) and V_{SD} (100 meV). The measurement is performed two months after the device fabrication was completed.

Section 6: Additional hysteresis data

Figure S6 shows the room temperature V_{BG} dependence of I_{SD} at fixed V_{TG} (0 V) and V_{SD} (100 meV) for a graphene contacted encapsulated BP device. The thickness of BP is ~ 6.5 nm. Similar to the data shown in manuscript, we observe nearly hysteresis free transport.

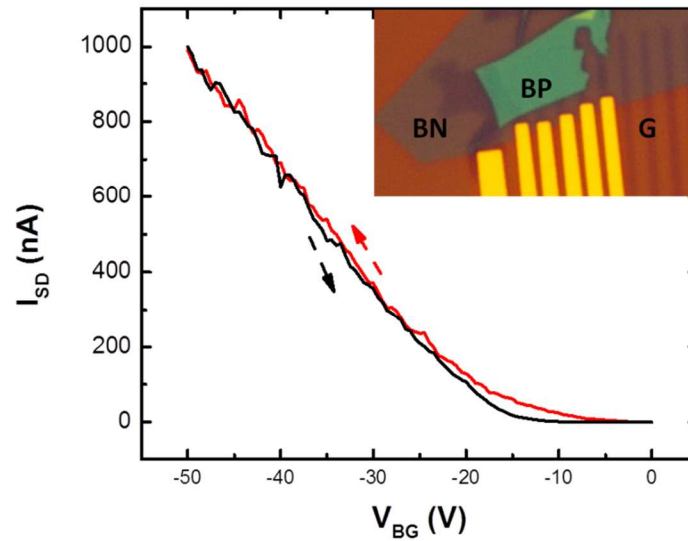


Figure S6: (a) Room temperature V_{BG} dependence of I_{SD} at fixed V_{TG} (0 V) and V_{SD} (100 meV). Red and black arrows represent the V_{BG} sweep directions. The inset shows the optical image of the measured device.

Section 7: Encapsulated devices contacted with Ti/Au contacts

As discussed in main text, the flexibility of monolayer graphene allows the BN passivation layer to seal BP very tightly. The graphene work function tunability results in ideal contact behavior. In order to test the performance of commonly used Ti/Au contacts in encapsulated BP device, we fabricated a Ti/Au (5nm/80nm) contacted BP-FET. A thin layer of BP (~6.5 nm) is exfoliated on SiO₂ substrate at glove box. A PMMA layer is span in glove box on the crystal for contact patterning and also to protect the sample from air during process. The surface of BP is exposed to the air at the contact regions after the resist development just before the metallization process. The lift off process is done in glove box followed by the transfer of a BN layer on top of the device. Figure S7-a shows the forward and backward scans of V_{BG} while I_{SD} is recorded. High hysteresis is observed in this device even it is encapsulated. This hysteresis is caused due to surface degradation at exposed contact area during the fabrication process. Non-flexible, thick Ti/Au contacts do not allow BN to seal BP perfectly, and samples degrades over time due to diffusion of gaseous from environment. Last but not least important, Ti/Au contacts do not show a linear relation between I_{SD} and V_{SD} even at low biases (Figure S7-b). All these results show the signficance of graphene contacts in the presented device architecture.

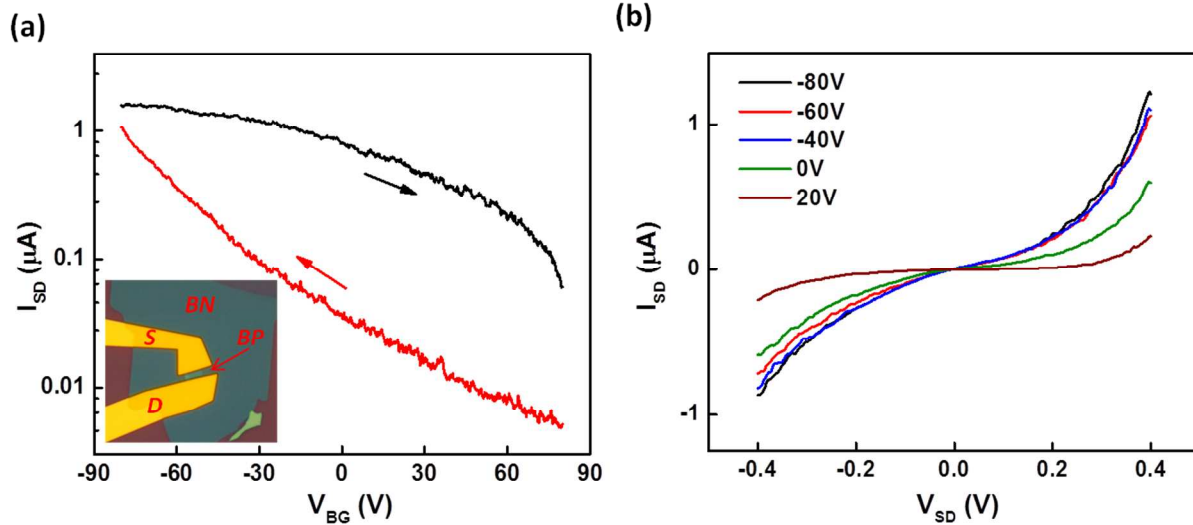


Figure S7: (a) Room temperature V_{BG} dependence of I_{SD} at fixed V_{SD} (100 meV) at vacuum conditions. Red and black arrows show the forward and backward sweep directions respectively. Inset: Optical image of Ti/Au contacted encapsulated BP device. (b) V_{SD} dependence of I_{SD} at fixed V_{BG} values.

Section 8: Discussion on the contribution of thermionic emission for the charge injection

Figure S8-a shows the Arrhenius plots recorded for $V_{BG}=50V$ while V_{TG} is kept fixed at $-4V$. Unlike previous reports which were utilizing Ti/Co metals as contact material², we observe negative slope for the Arrhenius plots at graphene contacted devices. The negative slope indicates that extracted Schottky barrier heights with the thermionic model are negative which clearly demonstrate that thermionic emission is not dominant in our graphene contacted devices (Figure S8-b). The observation of such extremely reduced Schottky barrier heights even at large V_{BG} values (displacement field is low) makes graphene contacts ideal for BP based FETs.

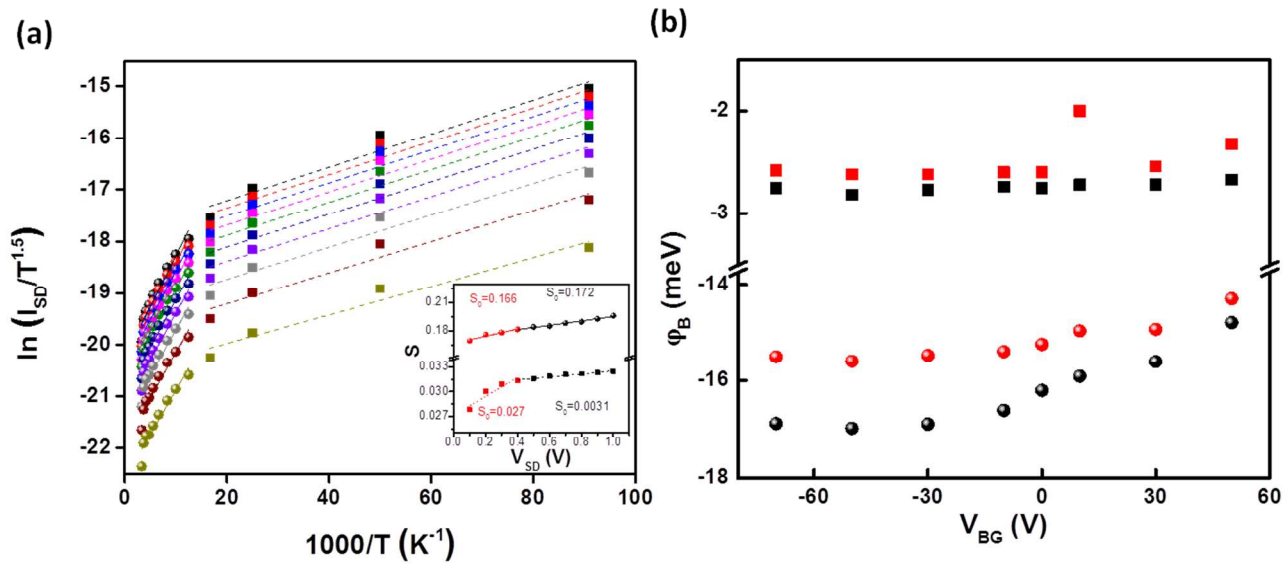


Figure S8: (a) Arrhenius plots of V_{SD} varying from 1V (Black) to 0.1V (Dark yellow) at $V_{BG}=50V$ and $V_{TG}=-4V$ respectively. (b) V_{BG} dependence of Schottky barrier height extracted from the Arrhenius plots at different temperature and bias ranges. Red and black squares represent the Schottky barrier heights at low (0.1V-0.4V) and high (0.5V-1V) V_{SD} values at low temperature range (11K-60K) respectively. Red and black spheres represent the Schottky barrier heights at low (0.1V-0.4V) and high (0.5V-1V) V_{SD} values at high temperature range (80K-300K) respectively.

Figure S9 shows the temperature and V_{BG} dependence of the I_{SD} - V_{SD} curve at fixed V_{TG} (-4V) for the ~ 4.5 nm thick encapsulated BP device, shown in manuscript. We note that temperature dependence of I_{SD} even at high positive V_{BG} is very weak and the charge injection is not dominated by the thermionic emission mechanism as discussed before in Figure S8.

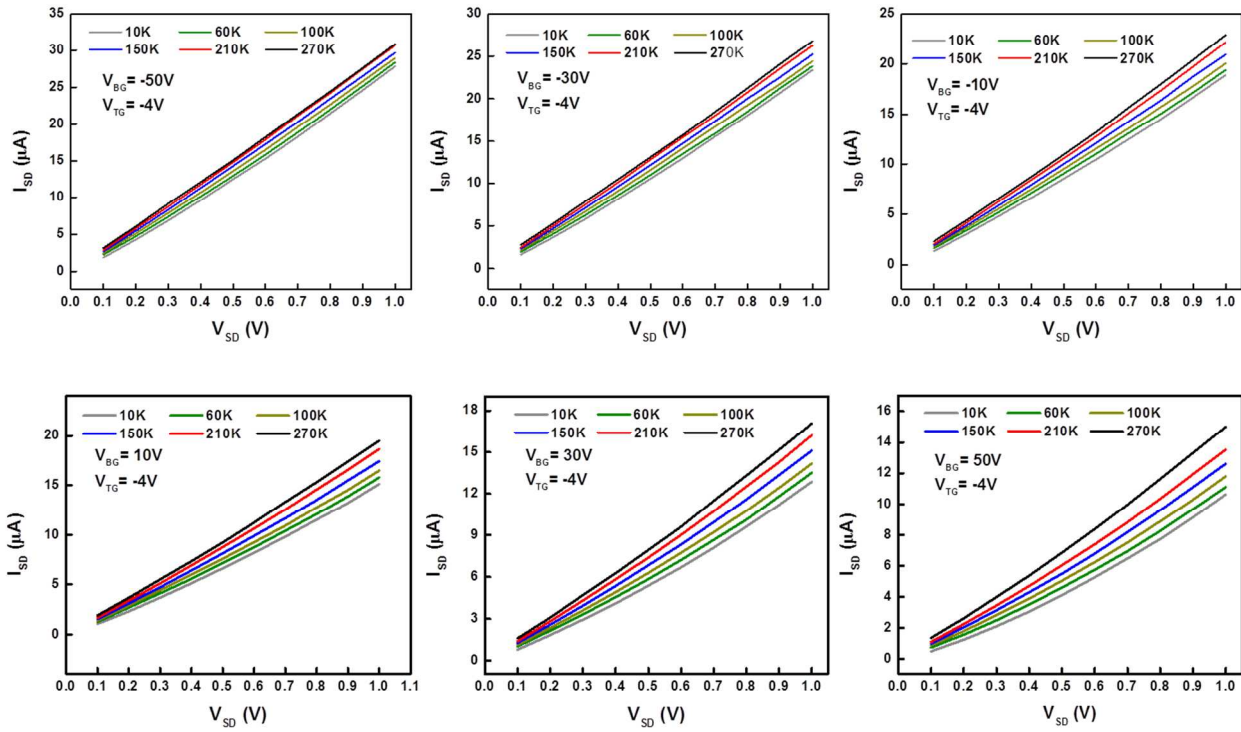


Figure S9: V_{SD} dependence of I_{SD} at different V_{BG} and temperature values.

Section 9: Work function tunability of graphene electrodes

As discussed in Figure 3 d-f, the application of vertical electric field tunes the work function of graphene⁵ and results in more effective charge injection into black phosphorous. This leads to a linear I-V at high negative displacement fields (both V_{BG} and V_{TG} negative). Here, we show the both V_{BG} and V_{TG} dependence of I_{SD} at room temperature. Similar to Figure 3-e, I-V deviates from perfect linearity as V_{TG} is swept from -4V to 4V.

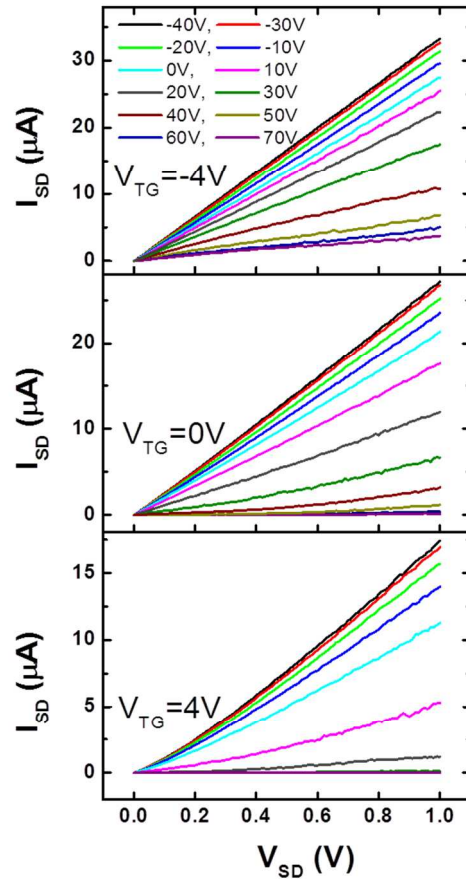


Figure S10: V_{SD} dependence of I_{SD} at different V_{BG} and V_{TG} at room temperature.

Section 10: Current modulation and subthreshold swing in encapsulated device

Figure S11-a shows the V_{TG} and V_{BG} dependence of I_{SD} at room temperature for the thicker device shown in manuscript. The device does not show the off state in V_{BG} sweep if $V_{TG} > -0.5V$. Figure S11-b shows the semi-log scale plot of I_{SD} vs V_{BG} at different V_{TG} values. The on/off ratio for this device exceeds 10^4 for hole charge carriers. Subthreshold swing is only ~ 2 V per decade. We note that the on/off ratio and subthreshold swing values are sample dependent, even shows variations at the different junctions in the same crystal. Figure S11-c shows the same plot for another encapsulated BP device. On/off ratio is $\sim 3.5 \times 10^3$ and subthreshold swing is ~ 4.5 V per decade. We note that the observed subthreshold swing values are slightly improved compared to the previous reports with similar thick SiO_2 dielectrics^{2,4}. Compared to MoS_2 FETs which have near-ideal subthreshold swings of ~ 70 mV/dec⁶, the larger values in our devices are mainly due to the thick SiO_2 dielectric used in our experiment. Thinner substrates with higher dielectric constants can significantly improve the subthreshold swing of BP.

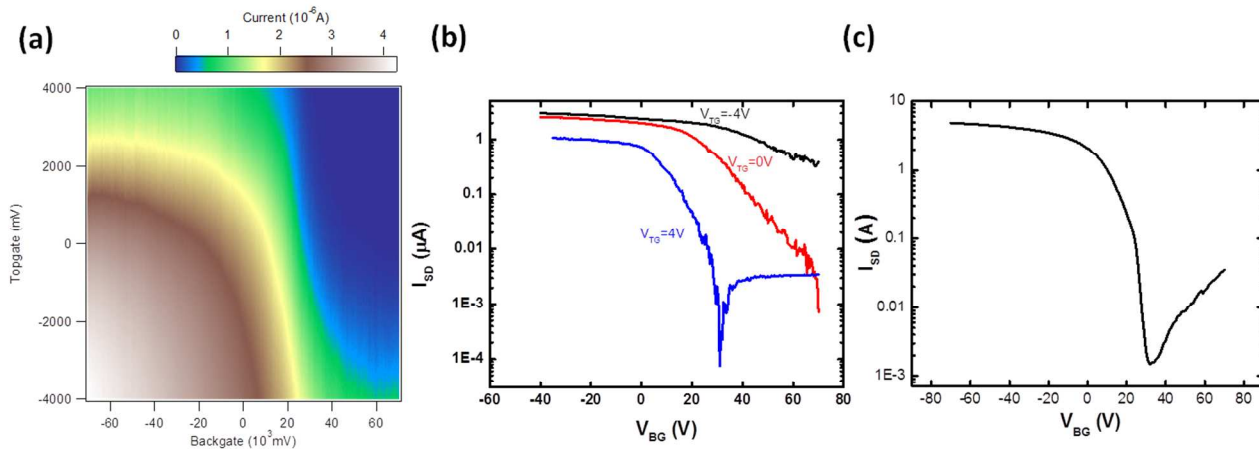


Figure S11: (a) V_{BG} and V_{TG} dependence of I_{SD} at fixed V_{SD} (0.1V) at room temperature. (b) Semi-log scale plot of I_{SD} as a function of V_{BG} at different V_{TG} values.

Section 11: Temperature dependent gate sweep of bias current in encapsulated device

Figure S12 shows the V_{BG} dependence of I_{SD} at different temperature values. V_{TG} (-4V) and V_{SD} (0.1V) are fixed during the measurement. The sample shows very weak temperature dependence because of the tunneling mechanism dominated charge injection rather than thermionic emission mechanism. The mobility of the device is measured at the slope where we observe very weak temperature dependence.

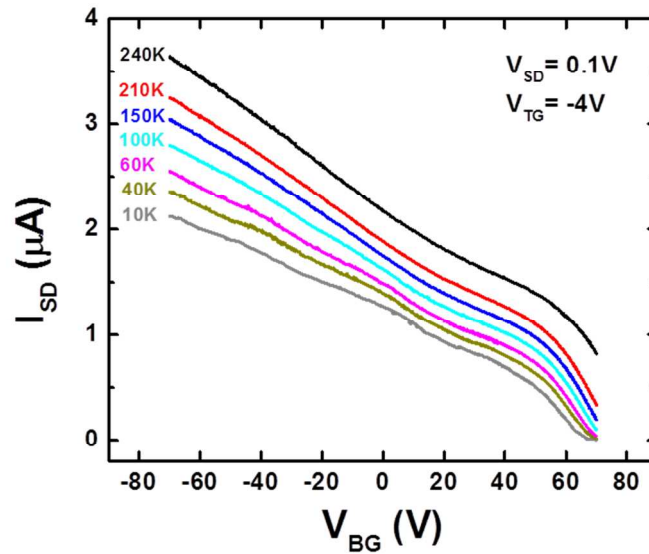


Figure S12: V_{BG} and temperature dependence of I_{SD} at fixed V_{TG} and V_{SD} values

REFERENCES

- (1) Wang, H.; Wu, Y.; Cong, C.; Shang, J.; Yu, T. *ACS Nano* **2010**, *4*, 7221–7228.
- (2) Kamalakar, M. V.; Madhushankar, B. N.; Dankert, A.; Dash, S. P. arXiv:1406.4476, **2014**.
- (3) Koenig, S. P.; Doganov, R. A.; Schmidt, H.; Castro Neto, A. H.; Özyilmaz, B. *Appl. Phys. Lett.* **2014**, *104*, 103106.
- (4) Li, L.; Yu, Y.; Ye, G. J.; Ge, Q.; Ou, X.; Wu, H.; Feng, D.; Chen, X. H.; Zhang, Y. *Nat. Nanotechnol.* **2014**, *9*, 372–377.
- (5) Yu, Y.-J.; Zhao, Y.; Ryu, S.; Brus, L. E.; Kim, K. S.; Kim, P. *Nano Lett.* **2009**, *9*, 3430–3434.
- (6) Kim, S.; Konar, A.; Hwang, W.-S.; Lee, J. H.; Lee, J.; Yang, J.; Jung, C.; Kim, H.; Yoo, J.-B.; Choi, J.-Y.; Jin, Y. W.; Lee, S. Y.; Jena, D.; Choi, W.; Kim, K. *Nat. Commun.* **2012**, *3*, 1011.